Surface Chemistry Hot Paper

How to cite: *Angew. Chem. Int. Ed.* **2021**, *60*, 16514–16520
International Edition: doi.org/10.1002/anie.202103359
German Edition: doi.org/10.1002/ange.202103359

Surface oxygen Vacancies on Reduced $Co_3O_4(100)$: Superoxide Formation and Ultra-Low-Temperature CO Oxidation

Yun Liu, Yuman Peng, Mathias Naschitzki, Sandy Gewinner, Wieland Schöllkopf, Helmut Kuhlenbeck, Rossitza Pentcheva, and Beatriz Roldan Cuenya*

Abstract: *The activation of molecular oxygen is a fundamental step in almost all catalytic oxidation reactions. We have studied this topic and the role of surface vacancies for $Co_3O_4(100)$ films with a synergistic combination of experimental and theoretical methods. We show that the as-prepared surface is B-layer terminated and that mild reduction produces oxygen single and double vacancies in this layer. Oxygen adsorption experiments clearly reveal different superoxide species below room temperature. The superoxide desorbs below ca. 120 K from a vacancy-free surface and is not active for CO oxidation while superoxide on a surface with oxygen vacancies is stable up to ca. 270 K and can oxidize CO already at the low temperature of 120 K. The vacancies are not refilled by oxygen from the superoxide, which makes them suitable for long-term operation. Our joint experimental/theoretical effort highlights the relevance of surface vacancies in catalytic oxidation reactions.*

Introduction

Co_3O_4, an antiferromagnetic mixed valence transition metal oxide with spinel structure, has versatile useful properties. It finds application as a blue pigment in pottery, as anode material in Li ion batteries[1,2] and also for gas sensing.[1,3] Beyond this, Co_3O_4 is an important material for catalytic applications. Ammonia oxidation,[4] CO oxidation,[5–15] water oxidation/OER (oxygen evolution reaction),[16–22] ORR (oxygen reduction reaction)[22,23] and hydrocarbon oxidation[24–26] are among the studied reactions. An attractive aspect of Co_3O_4 is its low cost as compared to catalysts based on precious metals, which are being employed as high performance catalysts for many of these reactions.

The role of surface vacancies and activated molecular oxygen on Co_3O_4 for the catalytic oxidation of CO at low temperature are in the focus of this manuscript. CO oxidation has been reported to occur already at 196 K on Co_3O_4 nanorods with (110) facets.[5] The authors claimed that Co^{3+} sites are the active centers, while for Co_3O_4 nanosheets with (111) termination[9] and mesoporous CoO_x[13,14] it was argued that Co^{2+} sites have this role. Some studies propose that surface vacancies play a role,[6,27] likewise an involvement of activated molecular oxygen species was proposed.[6,12] Studies on powder Co_3O_4 catalysts indicated the presence of several types of reactive oxygen species, but the nature of the different species and their role in catalytic reactions remained mostly unclear.[6,8,13,28,29] A clear spectroscopic evidence of the existence of activated oxygen species is still missing.[6,13,30,31]

Adsorbed activated molecular oxygen can supply oxygen for the CO oxidation, but also substrate lattice can do this.[32–34] In the latter case the task of the gas phase oxygen is to restore the catalyst by refilling the oxygen vacancies. This is a so-called Mars-van-Krevelen (MvK) mechanism and some authors report that this is the way how CO oxidation on Co_3O_4 proceeds.[5,7]

From this discussion it is clear that the current state of knowledge about the CO oxidation mechanism, the role of vacancies and the source of oxygen for the reaction is somewhat insufficient. Most of the cited studies have been performed on powder polycrystalline samples, which are more realistic systems than crystalline systems, but their inherent complexity often prevents a deeper understanding due to the manifold of processes occurring on the mostly hidden surfaces.

With the aim to provide new fundamental insight into structure–reactivity correlations, we have developed Co_3O_4-(100) thin film model catalysts supported on Au(100). The $Co_3O_4(100)$ surface is reported to be relevant for catalytic processes, but its structure has not yet been determined.[31,35–37] Therefore, regular vacancy-free $Co_3O_4(100)$ and reduced $Co_3O_4(100)$ surfaces were subjected to a structural characterization prior to the catalytic studies, using low-energy electron diffraction (LEED), scanning tunneling microscopy (STM), and density functional theory calculations including a Coulomb term (DFT + U) for the simulation of the STM images.

[*] Y. Liu, M. Naschitzki, H. Kuhlenbeck, B. Roldan Cuenya
Interface Science Department
Fritz-Haber-Institut der Max-Planck-Gesellschaft
14195 Berlin (Germany)
E-mail: kuhlenbeck@fhi-berlin.mpg.de
Y. Peng, R. Pentcheva
Department of Physics and Center for Nanointegration (CENIDE),
Universität Duisburg-Essen
Lotharstr. 1, 47057 Duisburg (Germany)
S. Gewinner, W. Schöllkopf
Molecular Physics Department
Fritz-Haber-Institut der Max-Planck-Gesellschaft
14195 Berlin (Germany)
Supporting information and the ORCID identification number(s) for the author(s) of this article can be found under: https://doi.org/10.1002/anie.202103359.

O_2 activation, CO oxidation and the effect of vacancies were investigated with temperature programmed desorption (TPD) and reaction (TPR), surface action spectroscopy (SAS), and DFT + U calculations. SAS is a novel vibrational surface spectroscopy method, able to identify surface and adsorbate structures via a fingerprint technique in combination with DFT vibrational modelling.[38]

In this study we cover the temperature range from ca. 100 K to 700 K to examine CO oxidation far below room temperature. We provide clear evidence of the relevant role of vacancies which stabilize superoxide species up to ca. 270 K and we show that the stabilized superoxide can oxidize CO already at 120 K via a mechanism that does not follow the Mars van Krevelen (MvK) paradigm.

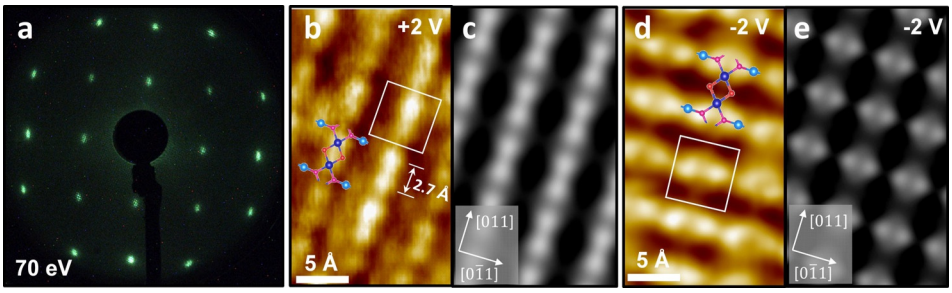

Figure 2. a) LEED pattern (70 eV electron energy) and b, d) high-resolution STM images of an as-oxidized Co_3O_4(100) film. b) was recorded with a positive and d) with a negative sample bias voltage. c),e) Simulated STM images (DFT + U) for B-layer terminated Co_3O_4(100) with positive (c) and negative (d) sample bias voltage. The unit cell structural motif and the surface unit cell (see Figure 1) are indicated in (b) and (d).

Results and Discussion

Figure 1a shows a top-view ball-stick model of a B-layer terminated Co_3O_4(100) surface and introduces the notation for the different types of surface atoms (consistent with Zasada et al.[39]) used throughout this text. O_{2O}, which bonds to two surface octahedral Co ions and a subsurface tetrahedral Co ion, and Co_{oct} are the topmost ions on the B-layer terminated Co_3O_4(100) surface. The O_{3O} ions connect to two surface and one subsurface octahedral Co ion. They are some tenth of an Å lower according to the DFT + U calculations. In the notation used throughout this text, O^1_{3O} would be an O_{3O} ion labeled with "1" in Figure 1a. (b) indicates the sequence of A- and B-layers along [100].

The surface structures of as-oxidized and mildly reduced Co_3O_4(100) were investigated with LEED and a combination of experimental and computed STM images. Figure 2a displays the LEED pattern of as-oxidized Co_3O_4(100). Sharp LEED spots and a low background intensity demonstrate that the surface is very well ordered and has a low defect density. There are no signs of surface reconstruction: the LEED surface unit cell corresponds to the real space unit cell indicated in Figure 1.

The high-resolution STM image in Figure 2b reveals that there are two protrusions with a distance of ca. 2.7 Å per unit cell. Commonly discussed terminations of Co_3O_4(100) are the A-layer termination, which has only one surface cation (Co_{tet}) per surface unit cell, and the B-layer termination, which has two cations (Co_{oct}),[8,30,35,37,39–42] see Figure 1. The brightest protrusions in the image simulated for a positive sample bias voltage, Figure 2c, are the Co_{oct} atoms. As expected, there are two atoms per unit cell, which are clearly visible also in the experimental image, Figure 2b. This observation is a first indication that the as-oxidized Co_3O_4(100) surface is terminated with a B-layer. The Co_{tet} ions are somewhat weaker in the simulation and they are also weakly visible in the measured image. To add further support to the hypothesis that the surface is terminated with a B-layer we have additionally recorded an STM image with a negative sample bias voltage, see Figure 2d, and computed the corresponding simulation, (e). The O_{2O} atoms are the brightest spots in the simulated image, followed by the Co_{oct} ions. This motif is also clearly visible in the STM image (d), which adds additional support to the interpretation that the surface is terminated with a B-layer, as previously also suggested by Arman et al. for a thin Co_3O_4(100) layer on Ag(100).[37] We note that the intensity strings in b and d are rotated by 90° with respect to each other since they are due to the O_{2O} ions at negative bias and to the Co_{oct} ions at positive bias. STM simulations for A- and B-layer terminated Co_3O_4-(100) are compared in the supporting information, Figure S2.

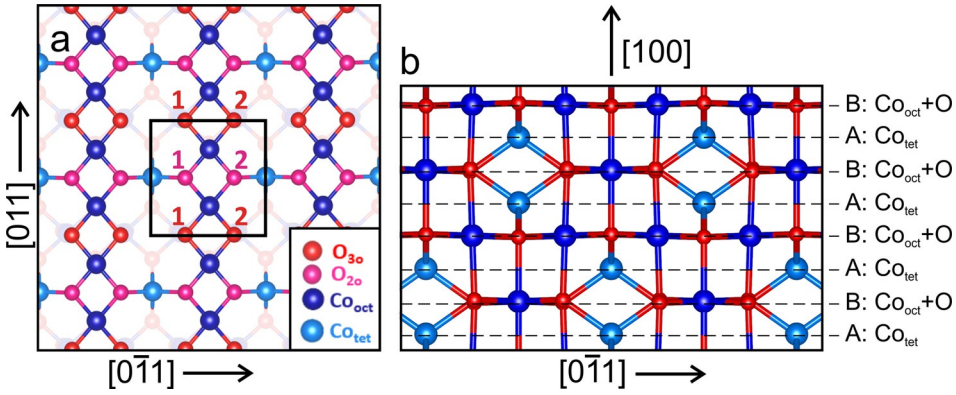

Figure 1. a) Ball-and-stick model of B-layer terminated Co_3O_4(100) with the surface unit cell indicated. The inset at the lower right introduces the notation used throughout this text for the different types of surface atoms. b) Side view indicating the sequence of A- and B-layers along [100] in bulk Co_3O_4.

A number of authors have computed surface phase diagrams of $Co_3O_4(100)$,[8,35,39,40,43,44] where the surface energy of differently terminated surfaces is plotted as a function of the oxygen chemical potential. A phase diagram computed in the context of this work is shown in the supporting information, Figure S3. The B-layer is oxygen-rich and, therefore, has a stability range towards elevated chemical potentials in most $Co_3O_4(100)$ surface phase diagrams,[8,35,39,40,43,44] starting at some negative potential. In view of our low $Co_3O_4(100)$ preparation temperature and the procedure of cooling the sample in an oxygen ambient atmosphere it is plausible that the as-oxidized surface is B-layer terminated, in agreement with previous results.[8,35,39,40,43,44]

As a next step we identify the nature of surface oxygen vacancies on the B-layer terminated $Co_3O_4(100)$; their surface stability is also shown in the phase diagram in Figure S3. Additionally, we have computed the formation energies of single and double vacancies with DFT + *U*, see Table 1.

Table 1: Computed formation energies of oxygen vacancies on a B-layer terminated $Co_3O_4(100)$ surface.[a]

Computational unit cell	Vacancy density (ML)	Type of vacancy	Formation energy [eV]
c(2×2)	1/8	$Vac(O_{3O})$	1.19
(1×1)	1/4	$Vac(O_{3O})$	1.52
(1×1)	1/4	$Vac(O_{2O})$	2.25
(1×1)	1/2	$Vac(O^1_{3O}, O^2_{3O})$	4.12
(1×1)	1/2	$Vac(O^1_{3O}, O^2_{2O})$	3.43

[a] The given energies are calculated as $\Delta E = E_{\text{B-layer with vacancy}} + 0.5\,E_{O2} - E_{\text{B-layer}}$ for a single vacancy and as $\Delta E = E_{\text{B-layer with double vacancy}} + E_{O2} - E_{\text{B-layer}}$ for a double vacancy. Results for a c(2×2) unit cell are included in order to show the effect of a vacancy density reduction. The notations "$Vac(O_{xx})$" and "$Vac(O^u_{xx}, O^v_{zz})$" denote one and two vacancies per unit cell, respectively. The superscripts *u* and *v* label the position in the unit cell, see Figure 1 a, where the oxygen vacancy is created.

Apparently, $Vac(O_{3O})$ has a smaller formation energy than $Vac(O_{2O})$, in agreement with some previous DFT calculations,[8,41] but at variance with others.[31,39] Double vacancies have higher formation energies since two oxygen atoms have to be removed. Nevertheless, they will form if the vacancy density exceeds 1/4 (a vacancy density of one is defined such that all four surface oxygen atoms in the unit cell are removed), in which case $Vac(O^1_{3O}, O^2_{2O})$ would be energetically favored. From these results one would expect that for vacancy concentrations of up to 1/4 ML, $Vac(O_{3O})$ dominates, and above this concentration $Vac(O^1_{3O}, O^2_{2O})$ is formed. This is also consistent with the appearance of these configurations in the surface phase diagram in Figure S3 in the Supporting Information.

LEED patterns and STM images combined with STM simulations were used to experimentally reveal the nature of the surface oxygen vacancies. The LEED image of a reduced thin $Co_3O_4(100)$ film, Figure 3 a, is different from that of the as-oxidized film, Figure 2 a, in that the (11) spots are missing. The missing spots become visible again at different electron energies (see supporting information, Figure S4). This means that the two-dimensional surface unit cells are identical for the as-oxidized and the reduced surfaces, but the atomic arrangements within the unit cells are different, as expected if oxygen ions are removed by annealing in vacuum. This would also lead to a shift of the cobalt atoms, which affect the LEED pattern more strongly than the oxygen atoms due to their higher scattering cross section, which may explain the complete removal of the (11)-type spots by reduction, see Figure 3 a. The absence of these spots also reveals that the reduction process did not just affect a small part of the surface but most of it.

Figure 3 c,e displays simulated STM images of $Co_3O_4(100)$ terminated with a B-layer having one $Vac(O_{3O})$ per unit cell for positive (c) and negative (e) sample bias voltages. As also found for vacancy-free $Co_3O_4(100)$, the Co_{oct} ions dominate the simulated image at positive sample bias voltage and at negative sample voltage O_{2O} prevails. However, due to the presence of the vacancy, the two O_{2O} ions have different intensities in Figure 3 e. The brightness difference of the two O_{2O} atoms in the simulated image is also seen in the upper part of the measured STM image shown in Figure 3 d, which supports the structural model put forward above. The bottom part shows a somewhat different structure, and the Supporting Information, Figure S4 g (Figure 3 d has been cut out from this Figure) in the supporting information reveals that a significant part of the surface is covered by this structure. We attribute this to a higher degree of reduction. If the degree of reduction is above 1/4 ML, then double vacancies, $Vac(O^1_{3O}, O^2_{2O})$, may form. These are the vacancies with the lowest formation energy according to Table 1. If the non-reduced phase would contribute significantly to the surface area, then the LEED pattern would exhibit intensity at the positions of the (11)-type spots, which is not the case. This is another indication that double vacancies occupy part of the surface area.

The effect of vacancies on the interaction with dioxygen was studied with TPD, SAS and DFT + *U*. As one may expect,

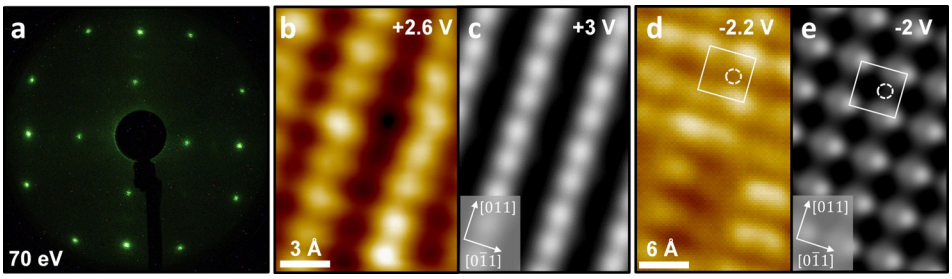

Figure 3. a) LEED pattern (70 eV electron energy) and b),d) high-resolution STM images of a reduced $Co_3O_4(100)$ film. Image (b) was recorded with a positive +2.6 V and (d) with a negative −2.2 V sample bias voltage. c),e) STM simulations (DFT + *U*) for B-layer terminated $Co_3O_4(100)$ with one $Vac(O_{3O})$ per unit cell for positive and negative sample bias voltages. The surface unit cell and the position of the O_{3O} oxygen vacancy (open circle) are indicated in (e).

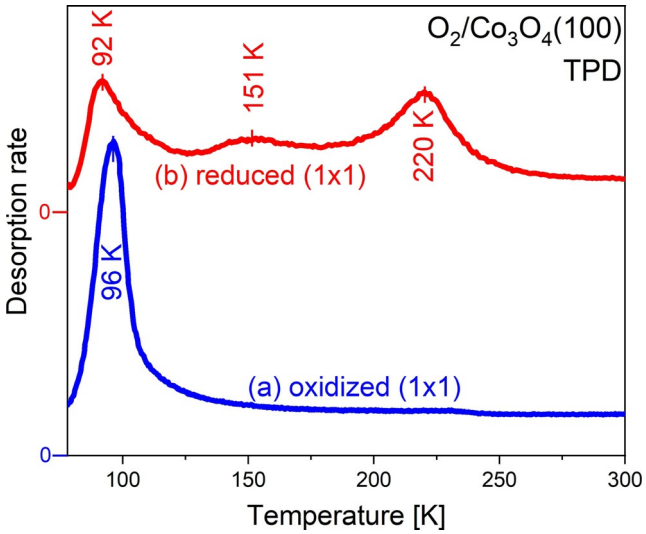

Figure 4. TPD spectra (heating rate = 1 $K s^{-1}$) of O_2 dosed at 80 K on as-oxidized (a) and reduced (b) $Co_3O_4(100)$ surfaces. The spectra have been displaced with respect to each other along the ordinate axis; the respective axis zero points are indicated.

O_2 binds differently to reduced and as-oxidized $Co_3O_4(100)$. TPD spectra (Figure 4) show that most molecular oxygen is desorbed below ca. 120 K from the as-oxidized surface, while O_2 is found up to ca. 270 K on the reduced surface. We estimate from these data that the average number of adsorbed oxygen molecules per $Co_3O_4(100)$ surface unit cell is 1.4 for reduced and 0.76 for as-oxidized $Co_3O_4(100)$. The three desorption maxima in the spectrum of the reduced surface are tentatively assigned to different adsorption sites and/or phase transitions within the adsorbate layer. To check whether there is an exchange of oxygen between the substrate lattice and the adsorbate we have performed a TPD experiment with $^{18}O_2$ on reduced $Co_3O_4(100)$ (see the Supporting Information, Figure S5), which shows that isotopic exchange with lattice oxygen does not occur.

The vibrational properties of the adsorbed oxygen were characterized with SAS, see Figure 5. The SAS spectra reflect the situation already indicated by the TPD spectra in Figure 4: at 190 K all O_2 has left the oxidized surface while a small signal of molecular oxygen is seen even at 270 K on the reduced surface. Peroxide (O_2^{2-}) vibrations are expected in an energy range of about 640 to 970 cm^{-1} and superoxide (O_2^-) vibrations are commonly identified between 970 and 1180 cm^{-1}.[33,45–47] Peroxide signals were not found, but both surfaces are able to activate molecular oxygen towards superoxide. Two superoxide states are identified for the as-oxidized and five for the reduced $Co_3O_4(100)$. To substantiate the assignment of these bands to superoxide O–O vibrations, a spectrum of a reduced surface exposed at 190 K to isotopic dioxygen, $^{18}O_2$, is also shown (spectrum (iv)). It is obvious that the vibrational energies are smaller, demonstrating that the vibrations are related to the adsorbed dioxygen. The energies of the line markers at the $^{18}O_2$ spectrum have been computed from the vibrational energies of $^{16}O_2$, spectrum (iii), using the harmonic oscillator approximation (see Figure caption). The experimental energies in spectrum (iv) fit quite well the calculated energies, which supports the assignment of the measured features to O–O vibrations.

The multitude of superoxide vibrational bands in Figure 5 may be attributed to different molecular states at the surface. This may include high-coverage states not included in the theoretical models but also molecules bound to surface structural defects and steps. Overall, we conclude that superoxide is stabilized on the reduced surface up to a temperature of about 270 K, while it is observed on the as-oxidized only up to ca. 120 K.

The adsorption of molecular oxygen on B-layer terminated $Co_3O_4(100)$ with and without vacancies has been modeled with DFT + *U*. Computed binding energies and O–O bond lengths are listed in Table 2. In agreement with TPD (Figure 4), the computed energies in Table 2 show clearly that dioxygen binds significantly more strongly to reduced surfaces. Reasonably strongly bound molecular oxygen is found on the reduced oxide for both, the lowest energy single and double vacancy [$Vac(O_{3O})$ and $Vac(O^1_{3O}, O^2_{2O})$]. A simple Redhead analysis[48] using an attempt frequency of 10^{13} s^{-1}, a heating rate of 1 $K s^{-1}$ and an O_2 desorption peak temperature of 220 K (see Figure 4) for the reduced oxide yields an O_2 desorption activation energy of 0.6 eV, which is in the range of the values compiled in Table 2 for single vacancies. We note that only a rough agreement between the Redhead values and the computed energies is expected since the latter are binding energies, while the Redhead equation computes desorption activation energies

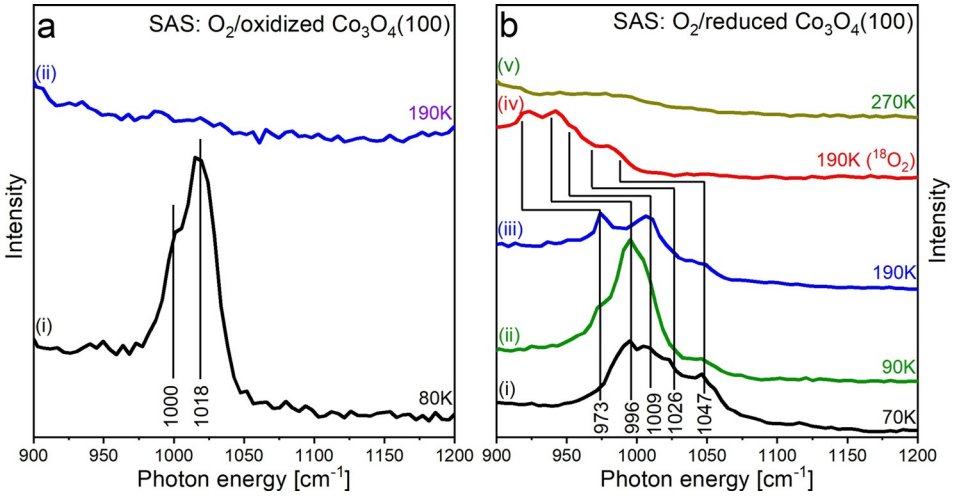

Figure 5. SAS spectra of an oxygen adsorbed layer on a) as-oxidized and b) reduced $Co_3O_4(100)$. Oxygen was dosed at the given temperatures. In (b) the spectrum of adsorbed $^{18}O_2$ is shown. The energies of the line markers at this spectrum have been calculated according to $E(^{18}O_2) = \sqrt{(8/9)}E(^{16}O_2)$.

Table 2: DFT + *U* computed adsorption energies and O–O bond lengths of molecular oxygen in different adsorption geometries on reduced (different vacancy configurations) and non-reduced B-layer terminated $Co_3O_4(100)$.[a]

Case	Vacancy type	Binding energy [eV]	O–O bond length [Å]
1	$Vac(O_{3O})$	−0.89	1.40
2	$Vac(O_{3O})$	−0.42	1.34
3	$Vac(O_{3O})$	−0.42	1.35
4	$Vac(O^1_{3O}, O^2_{2O})$	−1.07	1.39
5	$Vac(O^1_{3O}, O^2_{2O})$	−0.76	1.47
6	$Vac(O^1_{3O}, O^2_{2O})$	−0.62	1.34
7	$Vac(O^1_{3O}, O^2_{2O})$	−1.21	1.41
8	$Vac(O^1_{3O}, O^2_{2O})$	−0.40	1.47
9	No vacancy (B-layer)	−0.11	1.25

[a] The corresponding structures of cases 1, 7 and 9 are shown in Figure 6 and a full set of structures is presented in the Supporting Information, Figure S6.

(i.e. these energies include activation barriers) and the used attempt frequency is just a standard value. The Redhead equation yields a desorption activation energy of 0.25 eV for molecular oxygen on the as-oxidized surface, which is significantly smaller than the Redhead-computed value for dioxygen on the reduced surface, in agreement with the values listed in Table 2. Table 2 also lists O–O bond lengths. Values above ca. 1.45 Å are characteristic of peroxide[33] (cases 5 and 8 in Table 2), which has not been observed experimentally.

Figure 6 shows charge density difference plots and the surface structures before and after O_2 adsorption for those cases where the dioxygen is most strongly bound according to Table 2. Substantial electron density redistribution is observed in particular for the first two cases, where multiple cations in the surface and subsurface layer are involved, consistent with the strong bond of the O_2 molecules. The change of the magnetic moments reflects this charge rearrangement. The computed charge transfers from the oxide to the adsorbed O_2 molecule are 0.1 and 0.22 electron charges for the most strongly bound O_2 molecules on a single (case 1) and a double vacancy (case 7), respectively, which is in the range of values computed by other authors for superoxide.[41,49] Figure S6 in the SI displays ball-stick structural models for all cases in Table 2. Projected densities of state before and after adsorption are shown in Figure S7.

Several studies report that catalytic CO oxidation occurs at low temperature (< 300 K) on oxygen-treated Co_3O_4, and it was speculated that activated oxygen might be the responsible chemical species.[6,8,13,28,29] We have employed TPR to investigate this topic. In the experiments, the temperature was increased at a constant rate while maintaining a constant CO pressure. The present setup does not permit to measure the CO pressure directly at the sample surface, but from the pressure increase in the measuring chamber during the experiments we estimate that the CO pressure at the sample surface was in the 10^{-8} mbar range. The reaction products were detected with a QMS facing the sample. To minimize contributions of contaminations from the chamber background atmosphere to the spectra, we have used isotopic carbon monoxide ($^{13}C^{16}O$) and isotopic dioxygen ($^{18}O_2$) for this experiment, Figure 7.

Figure 7 shows $^{13}C^{16}O$ TPR data for as-oxidized and reduced $Co_3O_4(100)$ with and without $^{18}O_2$ pre-adsorption. Mass 47 ($^{13}C^{16}O^{18}O$) spectra are shown for surfaces pre-dosed with $^{18}O_2$ and for the surfaces without O_2 pre-dosage, mass 45 ($^{13}C^{16}O_2$) spectra are displayed, since in the latter case the production of $^{13}C^{16}O^{18}O$ is not expected. We note that the production of $^{13}C^{16}O_2$ was not observed for the surfaces pre-dosed with $^{18}O_2$.

The data reveal clearly that only reduced $Co_3O_4(100)$ with pre-dosed $^{18}O_2$ is active for CO oxidation below 700 K [spectrum (iv)] and that the reaction occurs already at the very low temperature of ca. 120 K. Obviously, the reduced surface is activated by dioxygen pre-dosing, while the oxidized surface cannot be activated in this way. The set of data shows, that both, vacancies and superoxide, are required for the low-temperature CO oxidation on $Co_3O_4(100)$, and that CO oxidation below 700 K does not occur via a MvK mechanism since the surfaces that were not exposed to $^{18}O_2$ are inactive.

For the reduced surface one might expect that the superoxide oxidizes the vacancies. If this were the case, then spectrum (iv) should be similar to spectrum (i) above ca. 300 K, since at this temperature the molecular oxygen is desorbed according to TPD (see Figure 4) and the surfaces would be identical (except for the incorporation of isotopic oxygen into the reduced surface). However, the spectra are clearly different. Furthermore, the (11)-type LEED spots do not reappear when the surface is treated with oxygen (see sup-

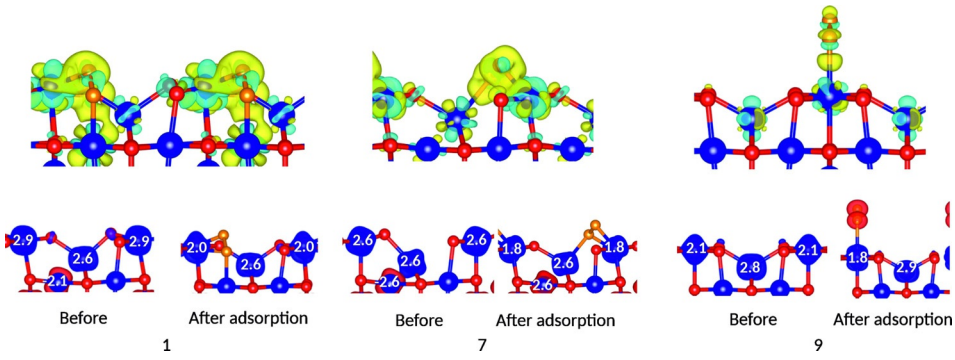

Figure 6. Top row: electron density difference plots indicating the re-arrangement of charge when molecular O_2 binds to $Co_3O_4(100)$ for those cases where O_2 is most strongly bound according to Table 2. Case 1: single vacancy per unit cell; case 7: two vacancies per unit cell; case 9: no vacancies (B-layer). The isosurface levels were set to ± 0.008 e Å^{-3}. Yellow: charge accumulation, cyan: charge depletion. The bottom row of images indicates the atomic positions before and after O_2 adsorption, and the spin densities. Substrate oxygen atoms are red, cobalt atoms are blue and the atoms of the adsorbed O_2 molecules are orange. Blue and red halos around the atoms correspond to positive/negative spin density and numbers are the magnetic moments of the respective Co ions in μ_B.

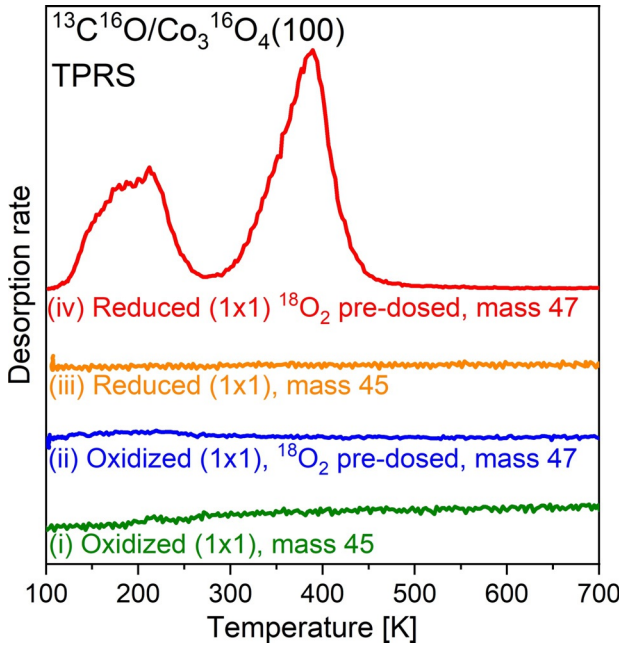

Figure 7. CO TPR spectra for (i) oxidized $Co_3O_4(100)$, detection of mass 45 ($^{13}C^{16}O_2$); (ii) oxidized $Co_3O_4(100)$ pre-dosed with $^{18}O_2$, detection of mass 47 ($^{13}C^{16}O^{18}O$); (iii) reduced $Co_3O_4(100)$, detection of mass 45 ($^{13}C^{16}O_2$); (iv) reduced $Co_3O_4(100)$ pre-dosed with $^{18}O_2$, detection of mass 47 ($^{13}C^{16}O^{18}O$). The $Co_3O_4(100)$ layer was prepared with $^{16}O_2$.

porting information, Figure S8), which demonstrates that the superoxide does not re-oxidize the vacancies. In order to further support this conclusion, we have performed three subsequent TPRS runs for reduced $Co_3O_4(100)$ pre-covered with oxygen (see supporting information, Figure S9), which reveal that the surface reactivity does not decline after TPRS. The robustness of the vacancies with respect to oxidation is an important parameter for continuous catalytic operation since it prevents quick deactivation. A possible reason for this robustness could be a large activation energy for superoxide dissociation.

According to the TPD (Figure 4) and SAS data (Figure 5) the superoxide is completely desorbed at ca. 270 K in case of a pure O_2 adsorbate, but there is apparently still CO_2 production above this temperature in spectrum (iv). This means that processes occurring below 270 K produce an environment which can oxidize CO even above 270 K. This reaction path is presently being investigated. First results point towards the presence of a complex intermediate species produced by the interaction of CO with the superoxide at low temperature.

For Co_3O_4 powder catalysts a correlation between the presence of defects and the catalytic activity was assumed by Yu et al.[6] In the present work we could explicitly demonstrate that it exists.

Conclusion

The structure of well-defined $Co_3O_4(100)$ thin films has been resolved with LEED and a combination of STM and DFT-based STM simulations. We could clearly show that as-oxidized $Co_3O_4(100)$ is terminated by a B-layer. Mild reduction leads to a surface with oxygen vacancies in the B-layer. According to the DFT + U calculations, O_{3O} single vacancies prevail for low vacancy concentrations, while Vac(O^1_{3O}, O^2_{2O}) double vacancies become relevant for higher degrees of reduction.

Both, the as-oxidized and the reduced surfaces are able to transform molecular oxygen into superoxide. SAS data reveal several different co-existing states at the surface. According to TPD, the activated oxygen desorbs below 120 K from the as-oxidized surface and below 270 K from the reduced one, consistent with computed O_2 adsorption energies. TPRS and LEED data show that the superoxide species do not re-oxidize the reduced surface, which is relevant for continuous catalytic operation.

The superoxide on the as-oxidized surface is not active for CO-oxidation, while the superoxide on the reduced surface is able to promote CO oxidation already at ca. 120 K. The surface remains active even above 270 K, the superoxide desorption temperature. Indications of a MvK reaction path below 700 K could not be found.

These results outline the critical role of oxygen vacancies for the catalytic activity of Co_3O_4: they are able to activate O_2 towards a superoxo form which acts as an oxygen supplier for CO oxidation. Our findings are highly relevant for the understanding of reactivity data on Co_3O_4 powder and to establish correlations between the presence of defects and the enhanced catalytic activity of the material.

Acknowledgements

Y.L. thanks the Alexander von Humboldt foundation for the postdoctoral fellowship and Y.P. thanks for support through the IMPRS SURMAT. Financial support from the Deutsche Forschungsgemeinschaft (DFG, German Research Foundation)—project no. 388390466—TRR 247, subproject A4 and B4 is also greatly appreciated. Finally, we gratefully acknowledge the provision of computational time at the Leibniz Rechenzentrum (project pr87ro). Open access funding enabled and organized by Projekt DEAL.

Conflict of interest

The authors declare no conflict of interest.

Keywords: Co_3O_4 · O_2 activation · oxide surfaces · oxygen vacancies · surface chemistry

[1] W. Y. Li, L. N. Xu, J. Chen, *Adv. Funct. Mater.* **2005**, *15*, 851 – 857.
[2] X. W. Lou, D. Deng, J. Y. Lee, J. Feng, L. A. Archer, *Adv. Mater.* **2008**, *20*, 258 – 262.

[3] H.-J. Kim, J.-H. Lee, *Sens. Actuators B* **2014**, *192*, 607 – 627.
[4] W.-K. Fung, L. Ledwaba, N. Modiba, M. Claeys, E. van Steen, *Catal. Sci. Technol.* **2013**, *3*, 1905 – 1909.
[5] X. Xie, Y. Li, Z.-Q. Liu, M. Haruta, W. Shen, *Nature* **2009**, *458*, 746 – 749.
[6] Y. Yu, T. Takei, H. Ohashi, H. He, X. Zhang, M. Haruta, *J. Catal.* **2009**, *267*, 121 – 128.
[7] L. Lukashuk, N. Yigit, R. Rameshan, E. Kolar, D. Teschner, M. Hävecker, A. Knop-Gericke, R. Schlögl, K. Föttinger, G. Rupprechter, *ACS Catal.* **2018**, *8*, 8630 – 8641.
[8] H.-F. Wang, R. Kavanagh, Y.-L. Guo, Y. Guo, G. Lu, P. Hu, *J. Catal.* **2012**, *296*, 110 – 119.
[9] Y. Teng, Y. Kusano, M. Azuma, M. Haruta, Y. Shimakawa, *Catal. Sci. Technol.* **2011**, *1*, 920 – 922.
[10] T. Baidya, T. Murayama, S. Nellaiappan, N. K. Katiyar, P. Bera, O. Safonova, M. Lin, K. R. Priolkar, S. Kundu, B. Srinivasa Rao, P. Steiger, S. Sharma, K. Biswas, S. K. Pradhan, N. Lingaiah, K. D. Malviya, M. Haruta, *J. Phys. Chem. C* **2019**, *123*, 19557 – 19571.
[11] L. Hu, K. Sun, Q. Peng, B. Xu, Y. Li, *Nano Res.* **2010**, *3*, 363 – 368.
[12] Y. Lou, Y. Cai, W. Hu, L. Wang, Q. Dai, W. Zhan, Y. Guo, P. Hu, X.-M. Cao, J. Liu, Y. Guo, *ACS Catal.* **2020**, *10*, 6094 – 6101.
[13] C.-J. Jia, M. Schwickardi, C. Weidenthaler, W. Schmidt, S. Korhonen, B. M. Weckhuysen, F. Schüth, *J. Am. Chem. Soc.* **2011**, *133*, 11279 – 11288.
[14] D. Gu, C.-J. Jia, C. Weidenthaler, H.-J. Bongard, B. Spliethoff, W. Schmidt, F. Schüth, *J. Am. Chem. Soc.* **2015**, *137*, 11407 – 11418.
[15] H. Kersell, Z. Hooshmand, G. Yan, D. Le, H. Nguyen, B. Eren, C. H. Wu, I. Waluyo, A. Hunt, S. Nemšák, G. Somorjai, T. S. Rahman, P. Sautet, M. Salmeron, *J. Am. Chem. Soc.* **2020**, *142*, 8312 – 8322.
[16] L. Xu, Q. Jiang, Z. Xiao, X. Li, J. Huo, S. Wang, L. Dai, *Angew. Chem. Int. Ed.* **2016**, *55*, 5277 – 5281; *Angew. Chem.* **2016**, *128*, 5363 – 5367.
[17] Z. Xiao, Y.-C. Huang, C.-L. Dong, C. Xie, Z. Liu, S. Du, W. Chen, D. Yan, L. Tao, Z. Shu, G. Zhang, H. Duan, Y. Wang, Y. Zou, R. Chen, S. Wang, *J. Am. Chem. Soc.* **2020**, *142*, 12087 – 12095.
[18] H.-Y. Wang, S.-F. Hung, Y.-Y. Hsu, L. Zhang, J. Miao, T.-S. Chan, Q. Xiong, B. Liu, *J. Phys. Chem. Lett.* **2016**, *7*, 4847 – 4853.
[19] J. Fester, A. Makoveev, D. Grumelli, R. Gutzler, Z. Sun, J. Rodríguez-Fernandez, K. Kern, J. V. Lauritsen, *Angew. Chem. Int. Ed.* **2018**, *57*, 11893 – 11897; *Angew. Chem.* **2018**, *130*, 12069 – 12073.
[20] J. Fester, M. García-Melchor, A. S. Walton, M. Bajdich, Z. Li, L. Lammich, A. Vojvodic, J. V. Lauritsen, *Nat. Commun.* **2017**, *8*, 14169.
[21] C. Stumm, M. Bertram, M. Kastenmeier, F. D. Speck, Z. Sun, J. Rodríguez-Fernández, J. V. Lauritsen, K. J. J. Mayrhofer, S. Cherevko, O. Brummel, J. Libuda, *Adv. Funct. Mater.* **2021**, *31*, 2009923.
[22] F. Buchner, M. Eckardt, T. Böhler, J. Kim, J. Gerlach, J. Schnaidt, R. J. Behm, *ChemSusChem* **2020**, *13*, 3199 – 3211.
[23] Y. Liang, H. Wang, P. Diao, W. Chang, G. Hong, Y. Li, M. Gong, L. Xie, J. Zhou, J. Wang, T. Z. Regier, F. Wei, H. Dai, *J. Am. Chem. Soc.* **2012**, *134*, 15849 – 15857.
[24] G. Salek, P. Alphonse, P. Dufour, S. Guillemet-Fritsch, C. Tenailleau, *Appl. Catal. B* **2014**, *147*, 1 – 7.
[25] F. F. Tao, J. Shan, L. Nguyen, Z. Wang, S. Zhang, L. Zhang, Z. Wu, W. Huang, S. Zeng, P. Hu, *Nat. Commun.* **2015**, *6*, 7798.
[26] E. C. Tyo, C. Yin, M. Di Vece, Q. Qian, G. Kwon, S. Lee, B. Lee, J. E. DeBartolo, S. Seifert, R. E. Winans, R. Si, B. Ricks, S. Goergen, M. Rutter, B. Zugic, M. Flytzani-Stephanopoulos, Z. W. Wang, R. E. Palmer, M. Neurock, S. Vajda, *ACS Catal.* **2012**, *2*, 2409 – 2423.
[27] M. V. Ganduglia-Pirovano, A. Hofmann, J. Sauer, *Surf. Sci. Rep.* **2007**, *62*, 219 – 270.
[28] S. Anke, G. Bendt, I. Sinev, H. Hajiyani, H. Antoni, I. Zegkinoglou, H. Jeon, R. Pentcheva, B. Roldan Cuenya, S. Schulz, M. Muhler, *ACS Catal.* **2019**, *9*, 5974 – 5985.
[29] J. Jansson, A. E. C. Palmqvist, E. Fridell, M. Skoglundh, L. Österlund, P. Thormählen, V. Langer, *J. Catal.* **2002**, *211*, 387 – 397.
[30] F. Zasada, W. Piskorz, J. Janas, E. Budiyanto, Z. Sojka, *J. Phys. Chem. C* **2017**, *121*, 24128 – 24143.
[31] F. Zasada, W. Piskorz, J. Janas, J. Gryboś, P. Indyka, Z. Sojka, *ACS Catal.* **2015**, *5*, 6879 – 6892.
[32] D. Widmann, R. J. Behm, *Acc. Chem. Res.* **2014**, *47*, 740 – 749.
[33] M. M. Montemore, M. A. van Spronsen, R. J. Madix, C. M. Friend, *Chem. Rev.* **2018**, *118*, 2816 – 2862.
[34] P. Ferstl, S. Mehl, M. A. Arman, M. Schuler, A. Toghan, B. Laszlo, Y. Lykhach, O. Brummel, E. Lundgren, J. Knudsen, L. Hammer, M. A. Schneider, J. Libuda, *J. Phys. Chem. C* **2015**, *119*, 16688 – 16699.
[35] L. Liu, Z. Cheng, Y. Li, J. Zhu, R. Yu, *J. Phys. Chem. C* **2020**, *124*, 25790 – 25795.
[36] Z. Zhang, X. Ke, B. Zhang, J. Deng, Y. Liu, W. Liu, H. Dai, F.-R. Chen, M. Sui, *J. Phys. Chem. Lett.* **2020**, *11*, 9913 – 9919.
[37] M. A. Arman, L. R. Merte, E. Lundgren, J. Knudsen, *Surf. Sci.* **2017**, *657*, 90 – 95.
[38] Y. Liu, Z. Wu, M. Naschitzki, S. Gewinner, W. Schöllkopf, X. Li, J. Paier, J. Sauer, H. Kuhlenbeck, H.-J. Freund, *J. Am. Chem. Soc.* **2020**, *142*, 2665 – 2671.
[39] F. Zasada, W. Piskorz, Z. Sojka, *J. Phys. Chem. C* **2015**, *119*, 19180 – 19191.
[40] A. Montoya, B. S. Haynes, *Chem. Phys. Lett.* **2011**, *502*, 63 – 68.
[41] K. Shojaee, A. Montoya, B. S. Haynes, *Comput. Mater. Sci.* **2013**, *72*, 15 – 25.
[42] G. S. Parkinson, *Surf. Sci. Rep.* **2016**, *71*, 272 – 365.
[43] A. H. Hashim, A. O. H. Zayed, S. M. Zain, V. S. Lee, S. M. Said, *Appl. Surf. Sci.* **2018**, *427*, 1090 – 1095.
[44] Y. Peng, H. Hajiyani, R. Pentcheva, *ACS Catal.* **2021**, *11*, 5601—5613.
[45] A. A. Davydov, N. Sheppard, *Molecular Spectroscopy of Oxide Catalyst Surfaces*, Wiley, Chichester, **2003**.
[46] C. Yang, X. Yu, S. Heißler, P. G. Weidler, A. Nefedov, Y. Wang, C. Wöll, T. Kropp, J. Paier, J. Sauer, *Angew. Chem. Int. Ed.* **2017**, *56*, 16399 – 16404; *Angew. Chem.* **2017**, *129*, 16618 – 16623.
[47] M. Che, A. J. Tench in *Advances in Catalysis* (Eds.: D. D. Eley, H. Pines, P. B. Weisz), Academic Press, New York, **1983**, pp. 1 – 148.
[48] P. A. Redhead, *Vacuum* **1962**, *12*, 203 – 211.
[49] A. Aniagyei, N. Y. Dzade, R. Tia, E. Adei, C. R. A. Catlow, N. H. de Leeuw, *Phys. Chem. Chem. Phys.* **2018**, *20*, 28685 – 28698.

Manuscript received: March 8, 2021
Revised manuscript received: April 26, 2021
Accepted manuscript online: May 17, 2021
Version of record online: June 18, 2021

